A&A manuscript no.
(will be inserted by hand later)

Your thesaurus codes are:
07 (08.01.1) (08.01.3)

ASTRONOMY AND ASTROPHYSICS

Detection of atmospheric velocity fields in A-type stars ⋆

J. D. Landstreet

Department of Physics and Astronomy, University of Western Ontario, London, Ontario, Canada N6A 3K7
and Observatoire Midi-Pyrénées, 14, ave. Edouard-Belin, 31400 Toulouse, France

Received December 29; accepted December 30,1999

Abstract. High signal-to-noise spectra with spectral resolution of more than 10^5 have been obtained of one normal B9.5V, one normal A1V, two Am stars, and two HgMn B stars having $v \sin i$ less than 6 km s^{-1}. These spectra are modeled with LTE line profile synthesis to test the extent to which the spectrum of each star can be modeled correctly with a single set of parameters T_e, $\log g$, chemical abundances, $v \sin i$, and (depth-independent) microturbulent velocity ξ. The answer to this question is important for abundance analysis of A and B stars; if conventional line synthesis does not reproduce the line *profiles* observed in stars of small $v \sin i$, results obtained from such analysis are not likely to be very precise.

The comparison of models with observations is then used to search for direct evidence of atmospheric motions, including line-strength dependent broadening, line core shape, and line asymmetries, in order to study how the microturbulence derived from abundance analysis is related to more direct evidence of atmospheric velocity fields.

It is found for the three stars with 12,000 $\geq T_e \geq$ 10,200 K (the normal star 21 Peg and the two HgMn stars 53 Tau and HD 193452) that ξ is less than 1 km s^{-1}, and line profiles are reproduced accurately by the synthesis with a single set of parameters.

The slightly cooler ($T_e \approx 9800$ K) star HD 72660 has only a slightly stronger surface convective layer than the hotter stars, but for this star $\xi \approx 2.2$ km s^{-1}. Strong spectral lines all show significant asymmetry, with the blue line wing deeper than the red wing, and have line bisectors which have curvature towards the blue with a span of about 0.5 to 1.0 km s^{-1}. A single model fits all lines satisfactorily.

The two Am stars (HD 108642 and 32 Aqr), with $T_e \approx$ 8000 K, are found to have much larger values of ξ (4 to 5 km s^{-1}). The strong spectral lines of these two stars are extremely asymmetric, with depressed blue wings, and the bisectors have spans of order 3 km s^{-1}. *No consistent fit to all lines can be found with a single model of the type used here.*

It is concluded (a) that classical LTE line synthesis is able to reproduce with considerable accuracy the line profiles of late B and early A stars with T_e above about 9500 K, but that the LTE model with depth-independent microturbulence provides a very poor approximation for cooler A stars, (b) that curve-of-growth microturbulent velocities in A stars are related to directly detectable atmospheric velocity fields, and (c) that the discrepancies between calculated and observed line profiles in stars with temperatures in the vicinity of 8000 K are so large that abundances derived mainly from saturated lines may well contain significant errors.

As a by-product, laboratory gf values for Fe II between 3800 and 5300 Å have been combined to form a set of data optimized for internal consistency of the gf values.

Key words: Stars: abundances – Stars: atmospheres

1. Introduction

The introduction of CCD and similar detectors has led to an enormous improvement in the linearity, dynamic range, and sensitivity available for high-resolution spectroscopy. It is now practical to obtain visible spectra having signal-to-noise ratios in excess of 300 at a resolving power of 10^5 or more for stars as faint as magnitude six, in which it is possible to resolve the intrinsic local thermal line profile of typical metal lines.

For stars of the middle main sequence, this increase in observational power opens up exciting possibilities. Most

⋆ Based on observations obtained with the Canada-France-Hawaii telescope, operated by the National Research Council of Canada, the Centre National de Recherche Scientifique of France, and the University of Hawaii, and with the 1.52-m telescope of the Observatoire de Haute Provence, operated by the Centre National de Recherche Scientifique of France.

Correspondence to: jlandstr@uwo.ca

A and B stars have such large projected rotational velocities ($v \sin i \sim 30$ - $300\ \mathrm{km\,s^{-1}}$ for "normal" stars and 10 - $100\ \mathrm{km\,s^{-1}}$ for "peculiar" stars) that it nearly impossible to extract any information about local line profiles from the rotationally broadened observed lines. However, a tiny fraction of the sample of nearby A and B stars is observed to have $v \sin i$ less than a few $\mathrm{km\,s^{-1}}$. It is now possible to study the line profiles of such stars, and to discover what information about conditions in the atmospheres is contained in these profiles.

In this paper I will examine what kinds of information may be obtained from high-resolution, high signal-to-noise ratio spectra of the sharpest-lined A and late B stars. The method of analysis will be to model the observed spectral lines using spectral synthesis in the observed (wavelength) domain. The goals of this programme are first, to see how accurately the observed spectrum of a sharp-lined A or B star can be fit by a single coherent LTE synthesis model; and secondly, to try to discover what further information may be contained in the profiles of lines, and in particular to discover what information may be present about atmospheric velocity fields.

2. Observations

Selection of extremely sharp-lined A and B stars cannot be done simply from previous studies. The lower limit of measured rotational velocities in most surveys is in the range of 5 to 15 km s^{-1}. I find that $v \sin i \approx 6$ km s^{-1} is about the largest projected rotational velocity which allows straightforward detection of features of the intrinsic line profile. To find such stars, I have re-observed the very sharpest-lined A and B stars from surveys such as those of Smith (1971), Wolff & Preston (1978), Boesgaard et al (1982), and Guthrie (1984) with resolving power R = 40,000 to 120,000. This work has been carried out using the Aurélie spectrograph at the Observatoire de Haute Provence (OHP), and the f/8.2 and f/4 coudé spectrographs at the Canada-France-Hawaii Telescope (CFHT).

A total of 18 non-magnetic A and B stars having observed line FWHM of less than 10 km s^{-1} (i.e. $v \sin i$ of less than 6 km s^{-1}) have so far been identified. This sample includes four apparently single stars, five single-lined and seven double-lined spectroscopic binaries, and two single-lined systems that are known to be speckle visual binaries. All the systems in which two stars contribute appreciably to the observed spectrum will be deferred to a later study, as analysis is substantially more complicated than for single stars. Of the nine apparently single or single-lined stars, I have spectra of sufficient signal-to-noise ratio for analysis for six. Two broader-lined stars are included to provide calibrations of gf values, comparisons with previous analyses, and information on how the value of $v \sin i$ affects the analysis.

The stars that will be analyzed are listed in Table 1, which gives the HD number, name, observed spectral type, and classification of each star as an apparently single (S) star or single-lined spectroscopic binary (SB1). (The star Sirius is a visual binary, but the secondary is so faint that it is undetected in visible-light spectra. The SB HD 108642 has recently been found to have a faintly detectable secondary spectrum [Wade et al 1998], but it is adequate to treat this system here as an SB1.) The final column of the table contains the observed full width at half maximum of typical spectral lines, based on Gaussian fits (uncorrected for the FWHM of 2.4 km s^{-1} of the instrumental profile). Note that these are not $v \sin i$ values.

Table 1. Stars analyzed in this study

HD	Name	Spectrum	Binary	FWHM (km s^{-1})
27295	53 Tau	B9 HgMn	SB1	7
47105	γ Gem	A0 IV	SB1	16
48915	Sirius	A1 V (Am)	VB	26
72660	HR 3383	A1 V	S	9
108642	HR 4750	A2m	SB1	6 – 12
193452	HR 7775	A0 III GaPt	SB1	4
209459	21 Peg	B9.5 V	S	6
209625	32 Aqr	A5m	SB1	8 – 16

To obtain information about the local or intrinsic (non-rotating) line profile, it is necessary to obtain spectra which resolve the local line even if it is broadened only by atomic thermal motions. For a typical iron peak element at 10,000 K, the mean thermal velocity is about 1.7 km s^{-1}, and the FWHM of a weak line with a thermal profile is about 2.9 km s^{-1}. To resolve this line we need $R > 1.0\,10^5$. The spectrographs of this resolving power at OHP and CFHT are both single-order instruments that yield spectra only 30 – 35 Å long. One must therefore choose the spectral region(s) to observe with care.

It is clear that a useful test of conventional spectrum synthesis is obtained from fitting the observed profiles of both weak and very strong resolved lines simultaneously. However, it is not *a priori* obvious what characteristics of the line profile will provide the most useful information about velocity fields that are not included in the line model of normal LTE spectrum synthesis. Following the discussions of Gray (1992) and Dravins (1987) we may anticipate that velocity fields could be detected through line profile asymmetries. Local turbulence might also be distinguished from stellar rotation by the characteristic shapes of the cores of the strongest lines. For both of these possibilities it is advantageous to have some strong lines in the spectral window(s). We also need to observe some weak lines in order to be able to evaluate accurately the true abundances and classical microturbulence. We thus look for spectral windows which contain a number of unblended lines of the dominant ion of one or more atomic species, having well-determined gf values and covering a wide range of equivalent width.

Because Fe II, Cr II and Ti II have large numbers of both weak and strong spectral lines in the optical spectral of A and late B stars, the spectra of these three ions were examined carefully. I chose a spectral window lying between 4615 and 4645 Å for most of the observations. The lines in this region are reasonably unblended in sharp-lined late B and early A stars. The region contains three fairly strong lines of each of Fe II and Cr II with well determined gf values.

The strongest metal lines in the visible are the Fe II lines of multiplet 42 at 4923, 5018 and 5169 Å. The regions containing these lines were not suitable as primary observing windows for this project because of they lack other lines with well-known atomic data, needed for determination of ξ. Nevertheless, exploratory observations were obtained of several stars in the 5169 Å line, for which a CFHT filter was available

Spectra used in this study have a resolution of about 120,000 (at 4630 Å) or 145,000 (at 5170 Å). Some were obtained during three observing runs (May 1993, February 1994, and September 1995) using the Aurélie spectrograph (Gillet et al 1994) on the 1.52-m telescope at OHP. The spectrograph was used with the 79 groove mm^{-1} echelle grating and an Andover Corp. 3-period interference filter of 55 Å FWHM centred at 4630 Å for order separation. The detector for this spectrograph is a one-dimensional "barrette" 1872 pixels long, built by Thomson CSF. The remaining spectra were obtained during three runs (March-April 1993, January 1995, December 1995) using the f/4 Gecko spectrograph at the CFHT. This spectrograph was used with the 316 groove mm^{-1} echelle mosaic grating, with the same 4630 Å interference filter, or with CFHT filter 1508. The detector used for the CFHT runs was the Loral 3, a 2048 pixel square thick CCD array.

All spectra were reduced using the IRAF image reduction package. The spectra were first cleaned to remove obvious cosmic rays. A number of columns on the Loral 3 CCD failed to read out correctly; the values for the corresponding extracted pixels were interpolated from adjacent columns. Next, background levels were subtracted from all science images (stellar, flat field, and tungsten hollow cathode spectra), based on separately measured short ("offset") and long dark integrations for the OHP one-dimensional array, and on mean background levels on the CCD above and below the observed spectrum for the CFHT data. Then each stellar spectrum was divided by a mean flat field obtained from observations of a quartz halogen lamp, and normalized to a continuum level of unity by division by a polynomial (typically of order six) fitted to the observed continuum. The spectra were calibrated in wavelength using observations of a ThAr hollow cathode lamp obtained before and after each stellar spectrum, and reduced to the heliocentric velocity frame of reference.

Comparison of spectra obtained from the various runs was very helpful in determining the quality of the data available, and in identifying and correcting problems with some of the spectra. Measurement of the FWHM of comparison spectral lines indicated that the resolving powers of the OHP and CFHT spectrographs at 4630 Å are almost exactly equal, which considerably simplified the task of comparing and combining spectra from the two instruments.

It is found that the overall wavelength calibrations of the two spectrographs agree to within about 0.5 km s^{-1}, and that when spectra from the two spectrographs are registered precisely, residual differences in wavelength calibration locally are generally less than 0.5 km s^{-1}. Similarly, the continuum level of the final spectra from the two spectrographs generally differ in intensity throughout the spectra by less than 0.5%.

Because order sorting was done with interference filters of less than 100 Å width, it was expected that the reduced spectra would have little scattered light compared to a conventional spectrograph, where (with order sorting filters $\sim 10^3$ Å wide) spectra are typically contaminated with roughly 4% scattered light. It was therefore surprising to discover that the spectra from OHP showed systematically weaker spectral lines than CFHT spectra; spectra of the same star could be made to coincide by making a scattered light correction to the OHP data of about the usual 4%. Therefore, the OHP spectra were corrected by subtraction of 0.04 from the continuum normalized spectra, followed by renormalization. It is assumed that the CFHT spectra do not need any scattered light correction. The origin of the residual background observed in the OHP spectra is not known; it may be due to an increase in the background level of the detector during stellar exposures compared to the level measured separately during dark exposures, or to relatively important near wings in the OHP instrumental profile.

In cases where more than one good spectrum of a particular star was available, spectra were combined to obtain a final spectrum of higher signal-to-noise ratio as follows. First, the spectra were registered in wavelength (which could involve a substantial wavelength shift in the case of an SB1). They were then averaged with weights proportional to the square of the estimated continuum signal-to-noise ratios. Resampling was done to the wavelength grid of the best spectrum.

The journal of wavelength window, Julian date JD, signal-to-noise ratio S/N, and source of spectra used in this study is given in Table 2. When more than one line is given for a single wavelength window, the corresponding spectra were combined as described above. Radial velocities v_{rad} observed for each spectrum are tabulated.

Table 2. Journal of spectra analyzed

HD	λ (Å)	JD (-2400000)	S/N	Tel	v_{rad} km s^{-1}
27295	4612 - 45	49401.304	125	OHP	+21
		49408.331	125	OHP	+4
		49986.577	100	OHP	+7
47105	4612 - 45	49078.910	250	CFH	-9
		49401.269	175	OHP	-10
48915	4612 - 45	49079.740	600	CFH	–
		49079.746	650	CFH	-8
72660	4612 - 45	50056.074	325	CFH	+3
	5155 - 85	49731.044	275	CFH	+3
108642	4612 - 45	50056.118	200	CFH	-42
	5155 - 85	49730.057	250	CFH	+10
193452	4612 - 45	50054.739	175	CFH	-18
	5155 - 85	50056.700	275	CFH	-19
209459	4612 - 45	50054.782	300	CFH	0
	5155 - 85	50056.736	300	CFH	0
209625	4612 - 45	50054.814	200	CFH	+17
	5155 - 85	50056,765	400	CFH	+13

3. Atomic data for line synthesis

The spectral window at 4630 Å contains enough reasonably unblended lines of Fe II and Cr II to make it possible to determine the curve-of-growth microturbulence and abundances for each of these elements. Accordingly, most of the lines in this window were synthesized. In contrast, the window at 5170 Å contains only one strong Fe II line, three resonance lines of Mg I, and two strong lines of Ti II; most of the window is blended with numerous weak lines of Fe I and II. For this window only the strong Fe II line was modeled.

Identifications were made from line synthesis using gf values from the line list of Hill & Landstreet (1993) and data from the Vienna Astrophysical Line Data-Base (VALD, Piskunov et al. 1995). All line profiles were computed as Voigt profiles, with radiative, van der Waals and Stark damping constants taken from the VALD data whenever available.

For accurate determination of the model microturbulent velocity ξ, it is particularly important to have *internally concordant* sets of gf values for the ions that are used to determine ξ, namely Cr II and Fe II. For Cr II, the oscillator strengths of multiplet 44 which appear in the 4630 Å window have been studied by Sigut & Landstreet (1990), who have shown that available data agree on a set of gf values that probably have less than 0.04 dex relative uncertainly (for the meaning of dex, see Allen 1973, p 7.). The gf values from this reference are used for all the low-excitation lines of Cr II.

For Fe II the situation is more complex. NIST evaluations exist for most of the stronger lines (Fuhr et al 1988), but the values of gf selected for each line do not come from a single homogeneous source, nor are they derived as averages over the best data sets. Instead, the Fe II gf values selected come from a variety of sources; for each line a single "best" value has been selected. This produces a set of gf values with good average normalization but poor internal consistency. Experiments with spectral synthesis show that these gf values are often in error by 0.10 dex or more. However, since laboratory gf values are available for a number of the strongest lines from several different experiments, it is possible to average these data to create a single homogeneous set of gf values of high internal consistency. As a byproduct, the uncertainty of individual relative gf values can also be estimated.

Table 3. Laboratory studies of Fe II in 3800 - 5400 Å (N: number of lines in λ interval; Δ: amount added to renormalize experiment to Bridges; σ: standard deviation of lines in common with Moity)

Reference	N	Δ	σ
Roder (1962)	17	-0.06	0.13
Baschek et al (1970)	13	+0.14	0.10
Wolnik, Berthel & Wares (1971)	12	-0.09	0.13
Bridges (1973)	7	(0.00)	-
Moity (1983)	54	+0.05	0.06
Kroll & Kock (1987)	20	-0.08	0.13
Whaling (listed by Fuhr et al 1988)	3	+0.12	0.17
Heise & Kock (1990)	6	+0.11	0.08

The method followed to combine the available Fe II data to form a single homogeneous set of gf values is similar to that employed by Ryabchikova et al (1994) to obtain a coherent set of oscillator strengths for Ti II, except that here, the combined data set for low-excitation lines is derived uniquely from laboratory measurements, without any use of astrophysical gf values. The experiments providing gf values that were used in the average set are listed in Table 3, where N gives the number of lines in the wavelength range 3800 – 5400 Å.

Following the recommendation of Fuhr et al (1988), the data of Bridges (1973) were used for overall absolute normalization. The large data set of Moity (1983) was first normalized to that of Bridges by addition of a constant to all the tabulated values of $\log gf$ so as to make the mean $\log gf$ for the seven lines in common between the two experiments equal. Then each of the other data sets was normalized by addition of a constant to all of the $\log gf$ values in that set so as to force the mean of all values in common with Moity to be the same as the mean of the same data set in Moity (as renormalized). The renormalization constant Δ added to the $\log gf$ values of each data set and the standard deviation σ of each set with respect to the lines in common with Moity are given in Table 3. (The Δ and σ given for Moity are with respect to the data of Bridges.) The fact that corrections of both positive and negative sign have to be added confirms that Bridges' work is a suitable standard for normalization, and the small size

Table 4. Mean laboratory $\log gf$ values for Fe II (*: uncertainty greater than 0.1 dex)

mult	λ(Å)	n	$(\log gf)_{av}$	σ_{int}	σ_{ext}
27	4173.461	2	-2.40*	0.14	0.07
28	4178.862	2	-2.52	0.04	0.07
27	4233.172	4	-1.90	0.06	0.05
27	4303.176	3	-2.52	0.04	0.06
27	4351.769	3	-2.17	0.04	0.06
27	4416.830	2	-2.46	0.03	0.07
37	4491.405	2	-2.72	0.06	0.07
38	4508.288	5	-2.32	0.03	0.04
37	4515.339	6	-2.47	0.01	0.04
37	4520.224	5	-2.59	0.04	0.04
38	4522.634	4	-2.15	0.02	0.05
37	4534.168	2	-3.36	0.01	0.07
38	4541.524	2	-2.80*	0.14	0.07
38	4549.474	3	-1.94	0.06	0.06
37	4555.893	3	-2.32	0.03	0.06
38	4576.340	3	-2.91	0.04	0.06
37	4582.835	3	-3.14	0.03	0.06
38	4583.837	7	-1.88	0.02	0.04
38	4620.521	3	-3.23	0.05	0.06
37	4629.339	6	-2.33	0.04	0.04
186	4635.316	1	-1.36		0.10
43	4731.453	2	-3.14*	0.12	0.07
42	4923.927	7	-1.36	0.04	0.04
42	5018.440	4	-1.23	0.05	0.05
42	5169.030	3	-1.03	0.04	0.06
49	5197.569	2	-2.24	0.06	0.07
49	5234.620	4	-2.14	0.02	0.05
49	5275.994	4	-2.06	0.02	0.05
49	5316.609	4	-1.87	0.05	0.05

of the corrections (typically 0.1 dex) indicates that all the experiments were reasonably well normalized. From the value of σ found from comparison of each set to that of Moity, I estimate that the internal standard error of each data set is of the order of 0.10 dex. (It has previously been shown by Ryabchikova et al [1994] that the internal standard error of the data of Moity is about 0.08 dex.)

The renormalized tables of $\log gf$ were then averaged for each spectral line. From the RMS deviation of the individual data an internal standard error σ_{int} for each mean $\log gf$ was derived, and assuming a standard error of 0.10 dex for each data set an external standard error σ_{ext} was obtained. Table 4 lists the multiplet number, the wavelength λ, the number n of data in each average, the resulting mean value $(\log gf)_{av}$, and the values of σ_{int} and σ_{ext} for all the lines between 3800 and 5400 Å for which more than one laboratory measurement is available. One $\log gf$ based on a single measurement, for λ 4635.316, is included. Other $\log gf$ values which appear in only one of these data sets can be put onto the scale adopted here by adding the correction given in Table 3. The full list of gf values is available from the author by e-mail.

The values of σ_{int} in Table 4 are almost always somewhat smaller than the values of σ_{ext}, probably because the errors of the various data sets are not accurately Gaussian, but have occasional distant outliers caused by instrumental problems, blends, etc. These outliers inflate the variance in the comparison of two data sets, and lead one to underestimate the relative accuracy of most of the lines. The three lines in Table 4 with $\sigma_{int} > 0.10$ ($\log gf$ values marked with *) are lines for which the two available measurements are quite discordant. It appears reasonable to assume that the value of σ_{int} gives a more accurate indication of the uncertainty of the relative $\log gf$ values than does σ_{ext}. The uncertainty is thus of the order of 0.05 dex for all but three lines in the table.

4. Spectrum synthesis

Spectrum synthesis of the observational spectra was carried out using a version of my magnetic synthesis code ZEEMAN, described by Landstreet (1988) and Landstreet et al (1989). The routine in this code for computing continuous opacity has been improved, and now includes Rayleigh scattering (treated as absorption) and He I bound-free and free-free absorption as well as bound-free and free-free absorption from both neutral H and H^-, and electron scattering. This code is specifically designed for synthesis of spectral lines in the presence of a magnetic field; it has no particular difficulty computing the spectrum with no magnetic field, but it runs slowly compared to a code designed for a non-magnetic atmosphere.

I have used a version of the code that searches automatically for a best fit to the observed spectrum, as judged by the RMS deviation between the calculated and observed spectrum in a defined region around the chosen spectral feature, by optimizing the choice of radial velocity v_r, projected rotational velocity $v \sin i$, and abundance $n(z)/n(H)$ of one specified element Z. A value for the microturbulent velocity ξ (constant through the atmosphere) is assumed. For this work, the surface is divided into 8 rings, and emergent intensities are computed for 216 surface elements of roughly equal area. The programme is run by a small UNIX shell script for a number of values of assumed ξ, and for each the best abundance is determined. The resulting abundance deduced from each line separately, as a function of assumed ξ, is plotted in a Blackwell diagram (see Fig. 1 below) from which the best value of ξ is chosen as the value which leads to the best agreement of abundances from different lines.

The model atmospheres used for this work have been computed using the ATLAS 9 code (Kurucz 1993) with experimental opacity distribution functions developed for the VALD project (Piskunov et al. 1995). The atmospheres were calculated with solar composition and a microturbulence of 2 km s^{-1}. A grid of models was kindly made available by N. Piskunov, with spacing of 250 K (500 K) in T_e below (above) 10000 K, and spacing of 0.5 in $\log g$. To obtain a model atmosphere for desired values of T_e and $\log g$, four models from the grid are selected with the nearest values of T_e and $\log g$ bracketing the desired values. It was found that an adequate model can be obtained by interpolating each depth level in the four models separately. At every level, the logarithm of each of the tabulated quantities is interpolated linearly within the grid of four "corner" models.

The accuracy of this interpolation scheme was tested by computing interpolated models using a set of "corner" models of sufficiently different T_e or $\log g$ that intermediate models exist in the available grid. Comparison of the interpolated models with the intermediate grid models of the same T_e and $\log g$ shows that the run of physical quantities as a function of surface mass density in the interpolated model differs from the intermediate model by negligible amounts for $T_e > 9000$ K. Below this effective temperature, significant differences begin to appear, but only deeper than an optical depth of about 5 in the spectral region of interest. This does not affect the emergent spectrum.

Choice of the values of T_e and $\log g$ for each star modeled was made using mean values of the Strömgren colours and β index obtained from the SIMBAD database. It is assumed that these (nearby) stars are unreddened. The Strömgren data are used to deduce appropriate values of T_e and $\log g$ from the revised grids of Smalley & Dworetsky (1994, 1995). These grids enable one to determine T_e with an uncertainty of the order of 300 K, and $\log g$ with an uncertainty of order 0.3 dex. The uncertainty in T_e and $\log g$ has little effect on any of the important conclusions of the paper concerning the existence (or not) of a single coherent model which adequately reproduces all modeled spectral features, or on the detection in the line profiles of traces of the atmospheric velocity field; the main effect of the uncertainties in fundamental parameters is to contribute to the uncertainties on the actual deduced values of abundance of Cr and Fe. Similarly, the use of a single value of ξ for all the atmosphere models used affects essentially only the deduced numerical values of abundance and ξ, but not the basic conclusions of the paper.

As a first test of the synthesis programme in this context, and to derive astrophysical gf values for high-excitation lines needed for this work, spectra were synthesized for the stars Sirius and γ Gem. These stars have substantially larger rotational broadening than other stars of this project, but both have accurately determined values of T_e and $\log g$, and are sufficiently sharp-lined to provide useful astrophysical gf values.

The atmospheric parameters derived for these two stars, together with those found below for the other stars, are given in Table 5. Both Sirius and γ Gem have fundamentally determined effective temperatures (Smalley & Dworetsky 1995). The gravity of Sirius has been determined extremely accurately from the astrometric orbit

Table 5. Model parameters for stars analyzed

HD	T_e	$\log g$	ξ	$\log \frac{n(\mathrm{Fe})}{n(\mathrm{H})}$	$\log \frac{n(\mathrm{Cr})}{n(\mathrm{H})}$	$v \sin i$
27295	11800	4.20	0.0	-5.40	-5.91	4.9
47105	9220	3.50	1.6	-4.60	-6.28	11.3
48915	9940	4.32	2.0	-4.23	-5.82	16.5
72660	9800	4.05	2.2	-4.20	-5.94	5.6
108642	8100	4.10	4.0	-4.49	-6.31	0.0:
193452	10500	4.10	0.6	-4.22	-5.72	1.4
209459	10200	3.50	0.5	-4.73	-6.44	3.9
209625	7900	3.90	4.5	-4.38	-6.13	1.0:

(Gatewood & Gatewood 1978), while that of γ Gem has been derived from an Hβ line profile fit (Smalley & Dworetsky 1995). Because these basic atmosphere parameters are accurately known, uncertainties in them do not contribute significantly to the uncertainties in other parameters.

For each of these stars all the significant lines in the 4630 Å window have been synthesized. Using the three strong lines of Cr II at 4616.629, 4618.803, and 4634.070 Å, for which precise relative gf values from Sigut & Landstreet (1990) are known, and the three Fe II lines at 4620.521, 4629.339, and 4635.316 Å using gf values from Table 4 above, the best value of ξ is determined by constructing Blackwell diagrams for a range of ξ between 0 and 3 km s^{-1}. The diagram for Sirius is shown in Figure 1. The Fe and Cr Blackwell diagrams for each star are completely concordant, and accurately define a very limited range of values for ξ. This concordance demonstrates that all six lines have accurately determined relative gf values. (Note that the value chosen used here for Fe II 4635.316, derived from the experiment of Moity [1983] with the same overall renormalization as all lines from this source [Table 3], is different from the value recommended by Fuhr et al [1988] by about 0.3 dex; their value is completely inconsistent with these spectra, even with the small renormalization needed to bring their recommended $\log gf$ values onto the scale I use. This result calls into question the large renormalization that Fuhr et al recommend for the high-excitation lines in Moity's experiment.) The deduced values of ξ, abundances $\log n(\mathrm{Cr})/n(\mathrm{H})$ and $\log n(\mathrm{Fe})/n(\mathrm{H})$, and $v \sin i$ are reported in Table 5.

As a next step, the gf values for the various weak high-excitation lines were corrected to give improved agreement between observed and calculated spectra. These weak lines are useful for defining correct abundances in some of the sharp-lined stars. Using Sirius and γ Gem, it was possible to correct the gf values of the Fe II line in multiplet 186 at 4625.893 Å and the strong line in multiplet 219 of Fe II at 4628.786. To obtain improved gf values for other weaker lines of Fe II and one weak line of Cr II, I synthesized the spectrum of the star HD 72660, using the atmospheric parameters from Table 5. The value of ξ and the abundances

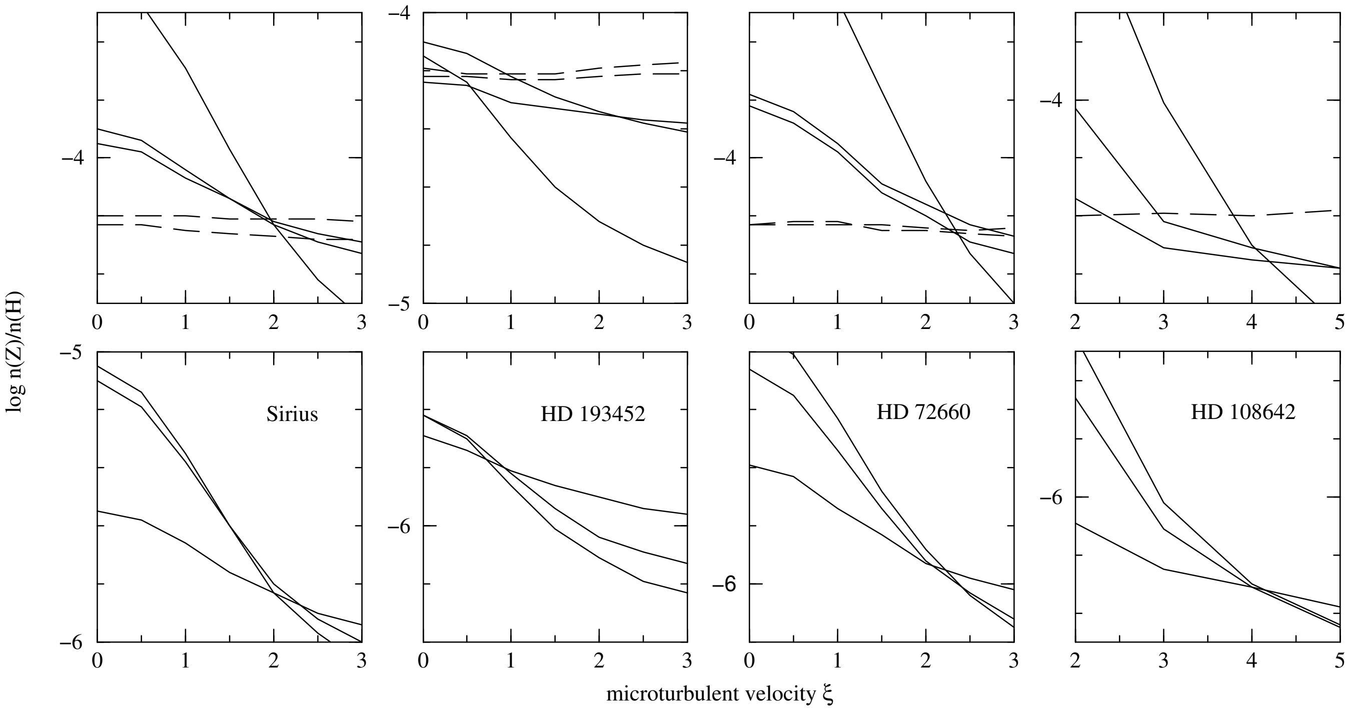

Fig. 1. Blackwell diagrams for (from left to right) Sirius, HD 193452, HD 72660, and HD 108642. The upper panels are for Fe II $\lambda\lambda$ 4620, 4625, 4629, 4635, and sometimes 4631; the lower panels are for Cr II $\lambda\lambda$ 4616, 4618, and 4634. Each panel is 1.0 dex high. Dashed curves indicate spectral lines with astrophysical gf values.

of Cr and Fe were determined from a Blackwell diagram (shown in Fig. 1) of the same Fe II and Cr II lines used for Sirius and γ Gem. The gf values found for $\lambda\lambda$ 4625.893 and 4628.786 Å fit the observed profiles well. Log gf values for the other high-excitation Fe II and Cr II lines were derived from the spectrum of HD 72660. Although T_e and $\log g$ are not determined as accurately for HD 72660 as for Sirius and γ Gem, the fact that the gf values of the weaker Fe II lines are determined relative to lines of similar excitation means that the relative gf values of these weaker lines are insensitive to errors in the atmospheric parameters of HD 72660.

Table 6 presents the full list of lines used in the synthesis of the spectral windows modeled. The oscillator strengths which have been adjusted astrophysically are marked with asterisks. The standard error of the astrophysical $\log gf$ values of Fe II lines is estimated to be about 0.10 dex, except for the line at 4638.050 Å, which is blended with a line of Fe I, and has an uncertainty of about 0.20 dex. The standard error of the λ 4616.241 Cr II line is estimated to be about 0.15 dex relative to the lines of multiplet 44.

5. Line profiles

5.1. The standard stars Sirius and γ Gem

We now turn to a comparison of synthesized and observed line profiles. We consider first the line profiles of Sirius and γ Gem. Most of the profiles synthesized for these two stars are shown, together with similar profiles for the other stars studied, in Figures 2 (for features primarily due to Cr II) and Figures 3 and 4 (for features primarily due respectively to strong and weak lines of Fe II). The figures as plotted are all for a single set of model parameters (T_e, $\log g$, $v \sin i$, ξ, and abundances) for each star; the line profiles do not have individually tuned values of $v \sin i$, abundance, or ξ. In all plots, the assumed value of ξ is that deduced from the Blackwell diagrams.

It is clear that the shapes of all lines in both these relatively rapidly rotating stars are synthesized reasonably accurately. However, small discrepancies exist. For Sirius, the best fitting values of $v \sin i$ range between 16.2 and 16.4 for the weaker lines synthesized (Cr II λ 4616, Fe II $\lambda\lambda$ 4620 and 4635), but for the three strongest lines (Cr II $\lambda\lambda$ 4618 and 4634 and Fe II λ 4629) the best fit $v \sin i$ values lie between 16.6 and 16.7 km s^{-1}. In the present plots, calculated for a single value of $v \sin i = 16.5$ km s^{-1} and $\xi = 2.0$ km s^{-1}, this discrepancy takes the form of theoretical profiles which are very slightly wider and shallower than the observed lines for the weaker lines (e.g. Fe II λ 4635), but slightly narrower and deeper than the profiles of the strong lines (e.g. Cr II λ 4618, Fe II λ 4629). The effect is marginal at the scale of the figures here. A second, also very small, difference is seen close to the continuum, where a few observed lines have slightly

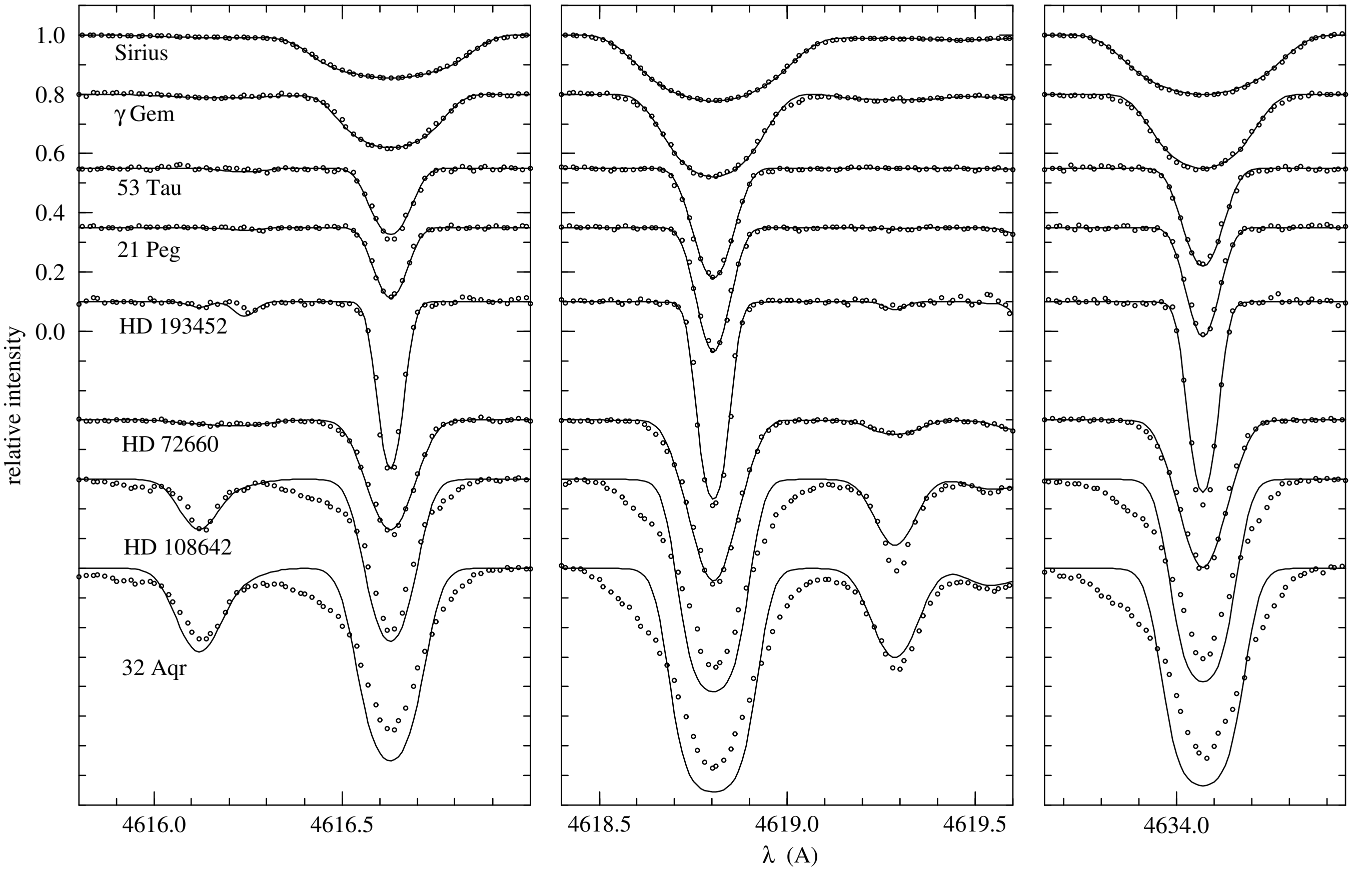

Fig. 2. Comparison of observed (dots) and calculated (solid lines) line profiles for the three strong lines of Cr II $\lambda\lambda$ 4616, 4618, and 4634 Å. All observations have been shifted to the radial velocity frame of reference of the laboratory for ease of plotting. From top to bottom, the profiles are for HD 48915 (Sirius), HD 47105 (γ Gem), HD 27295 (53 Tau), HD 209459 (21 Peg), HD 193452, HD 72660, HD 108642, and HD 209625 (32 Aqr).

deeper wings than the calculated lines (e.g. Cr II $\lambda\lambda$ 4616, 4618).

Comparison of observed and calculated profiles of γ Gem reveals similar differences, but in this star the differences are large enough to be visible on the figures. Again there is a clear trend for the best fit value of $v \sin i$ to increase with line strength, from values between 11.0 and 11.2 km s^{-1} for weaker lines, up to 11.8 km s^{-1} for the strongest line Fe II λ 4629. This is visible in the plots, all calculated for a single model with $v \sin i = 11.3$ km s^{-1} and $\xi = 1.5$ km s^{-1}, as calculated profiles which are slightly wider and shallower than the observed weaker lines Cr II λ 4616, Fe II $\lambda\lambda$ 4620 and 4635, and a calculated profile that is slightly too narrow and deep for Fe II λ 4629. For this star, the occurrence of wings close to the continuum that are slightly deeper in the observed lines than in the calculated profiles is easily visible in Figures 2 and 3.

Overall, the agreement between observed and synthesized line profiles for these two stars is good but not perfect. It seems likely that the small discrepancies observed between calculated and observed line profiles are due to an inadequate description of the atmospheric velocity field in the standard line synthesis model used here. (For example, the velocity field may depend on height in the atmosphere in a way that affects lines of different strengths differently.) If this is correct, even with values of $v \sin i$ as large as those found for Sirius and γ Gem, there appears to be usable information in the line profiles about these velocity fields.

5.2. The stars 53 Tau, HD 193452, and 21 Peg

We next consider together the three stars with effective temperatures of more than 10,000 K. These three stars all have quite small values of ξ as determined from the Blackwell diagrams. The atmosphere parameters adopted are listed in Table 5. For each star, the spectrum synthesis programme was used to find, line by line, the values of v_r, $v \sin i$, and abundance $\log n(\mathrm{Cr})/n(\mathrm{H})$ or $\log n(\mathrm{Fe})/n(\mathrm{H})$ that best fit the line profile, for a series of assumed microturbulent velocities ξ ranging from 0 to 3 km s^{-1} in steps of 0.5 km s^{-1}. The resulting deduced values of abundance as a function of ξ were plotted for all modeled lines, and

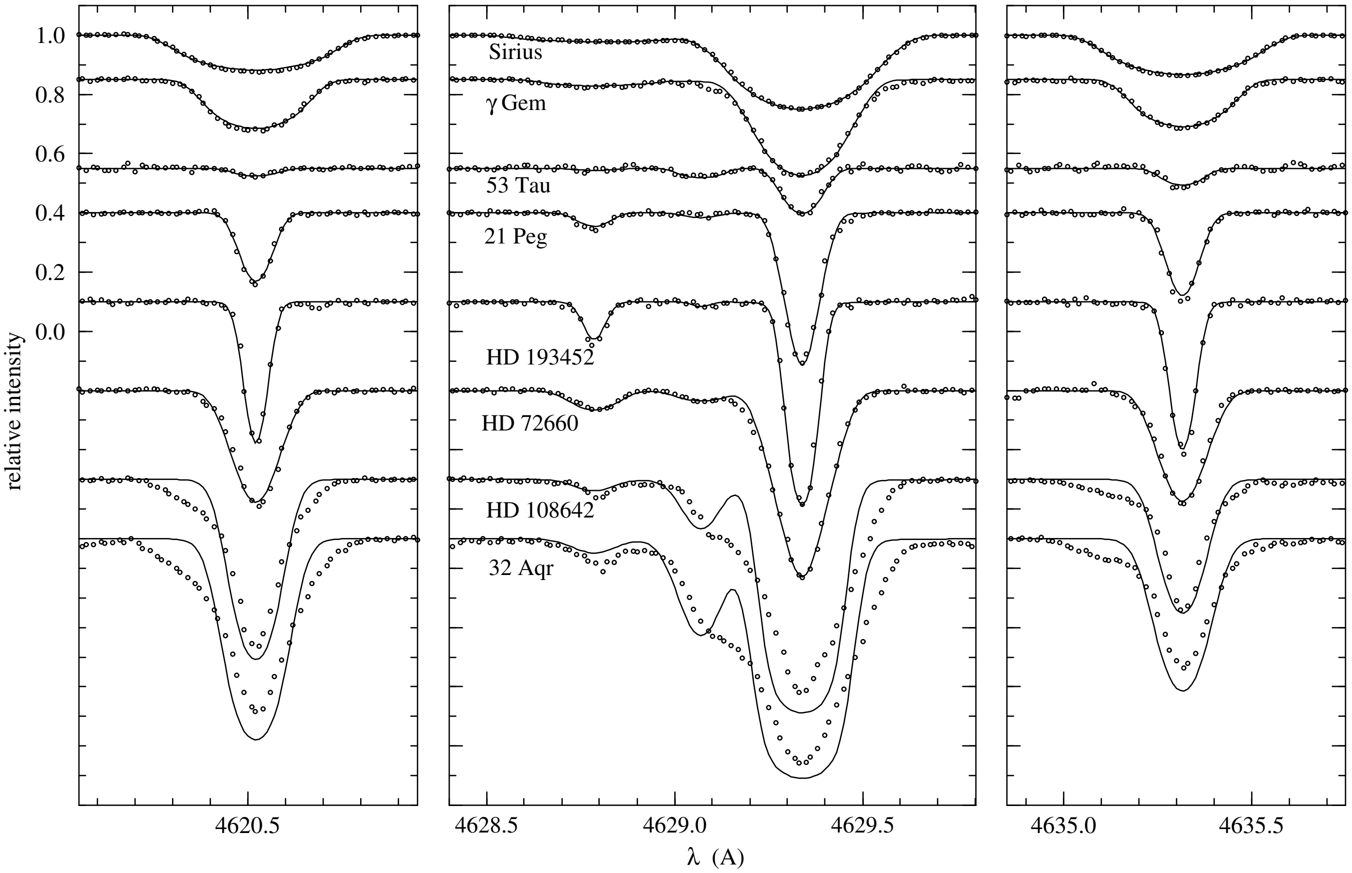

Fig. 3. Comparison of observed (dots) and calculated (solid lines) line profiles for three strong lines of Fe II $\lambda\lambda$ 4620, 4629, and 4635 Å. From top to bottom, the profiles are for HD 48915 (Sirius), HD 47105 (γ Gem), HD 27295 (53 Tau), HD 209459 (21 Peg), HD 193452, HD 72660, HD 108642, and HD 209625 (32 Aqr).

the best choice for ξ was determined. The Blackwell diagram for HD 193452 is shown in Figure 1.

The Blackwell diagrams for all three stars show a similar level of concordance. Typically, the value of ξ is determined to within 0.2 to 0.5 km s^{-1}; for all three stars most lines are in good agreement on the best value of ξ but the curves for one or two lines deviate from the rest by an amount which at worst is nearly 0.1 dex. Such deviations seem to result from a combination of small errors in continuum placement, photometric errors in line profiles (the weaker lines have relative errors of the order of 10% of the continuum), and probably the limitations of the model of line profiles used. They do not occur in a systematic manner that suggest that further adjustment of gf values is needed.

The deduced values of ξ are given in Table 5, along with the inferred Cr and Fe abundances. For 53 Tau, ξ is constrained only by the Cr lines, because the abundance of Fe is so low (roughly 1 dex lower than solar) that none of the Fe lines are significantly saturated! A value of $\xi = 0$ km s^{-1} is adopted for this star; the limit from the Blackwell diagram is simply $\xi \leq 1$ km s^{-1}. For HD 193452, the adopted value $\xi = 0.6$ km s^{-1} is the value which gives the best overall concordance for Fe and Cr, but ξ could have any value between 0 and 0.8 km s^{-1}. In 21 Peg, the Cr lines constrain ξ to less than about 0.8 km s^{-1}. The Fe lines suggest a value of not much more than 0.6 km s^{-1}. The adopted 0.5 km s^{-1} is (marginally) the best fit, but any value of ξ between 0.0 and 0.6 km s^{-1} is acceptable.

For each of these three stars, the adopted value of ξ was used to refit the lines and determine for each the best fit values of $v \sin i$. For 53 Tau and 21 Peg, the deduced values of $v \sin i$ are extremely concordant. Typically the dispersion from line to line is of order 0.1 to 0.2 km s^{-1}, with one or two outliers (weak lines which can be strongly affected by small photometric errors) differing by 0.5 km s^{-1} from the rest. The dispersion for HD 193452 was somewhat larger, about 0.4 km s^{-1}, but this simply reflects the difficulty of determining the value of $v \sin i$ when the FWHM of the rotational profile is significantly less than the FWHM of the instrumental profile.

Final line profiles were calculated with the ξ and $v \sin i$ values of Table 5, and are shown in Figures 2 – 4. All of the calculated profiles are in excellent general agreement with the observed profiles, except for small errors in line depth which are due to the fact that we have used a single

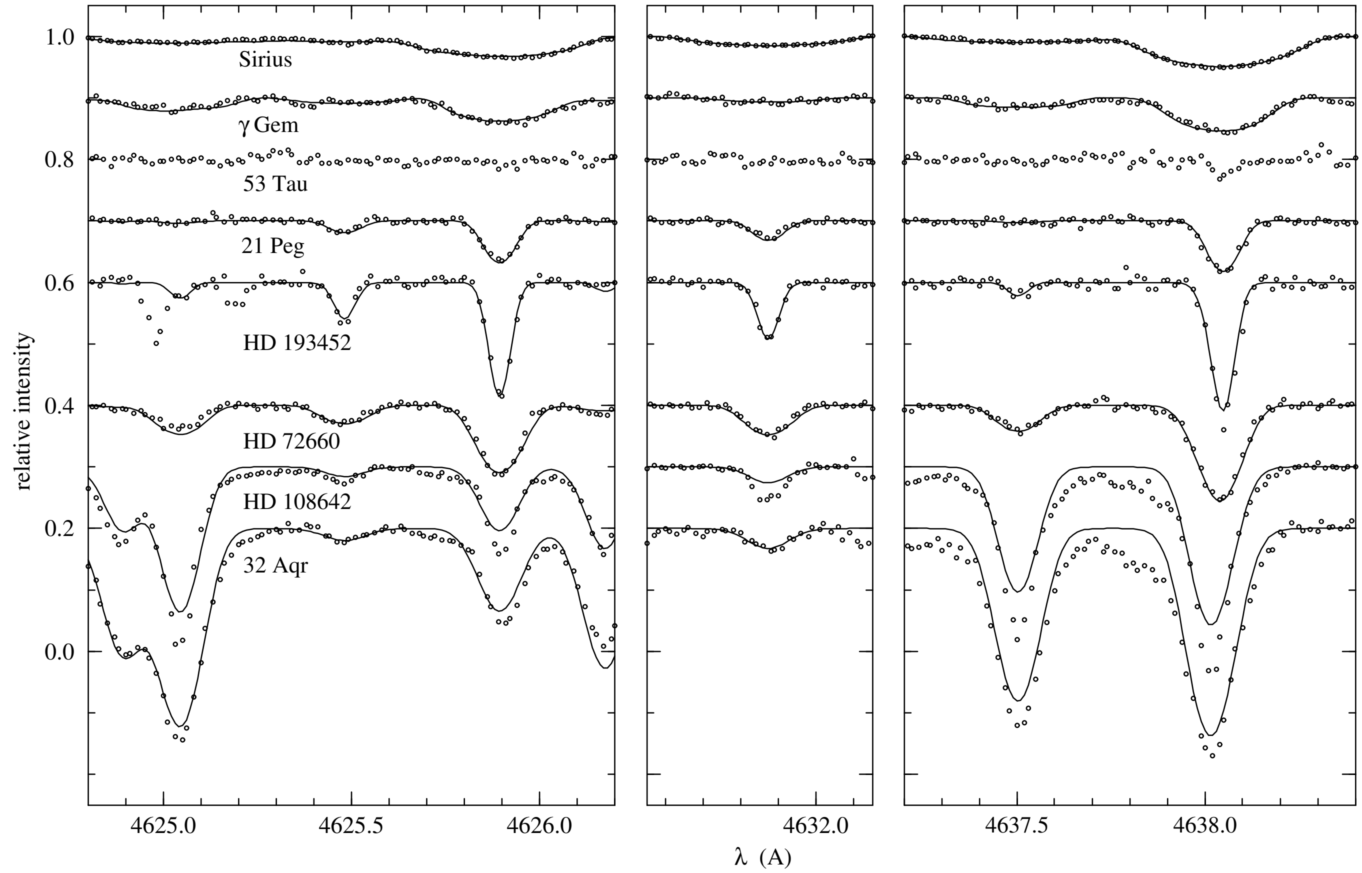

Fig. 4. Comparison of observed (dots) and calculated (solid lines) line profiles for three windows containing the weak Fe II lines $\lambda\lambda$ 4625, 4631, and 4637 Å. Notice that the vertical scale is expanded by a factor of 2 relative to the scale employed for strong lines. From top to bottom, the profiles are for HD 48915 (Sirius), HD 47105 (γ Gem), HD 27295 (53 Tau), HD 209459 (21 Peg), HD 193452, HD 72660, HD 108642, and HD 209625 (32 Aqr). No spectrum was computed for HD 27295 for these lines because they are too weak.

value of $v \sin i$ and a single abundance table to calculate all the profiles for each star. Somewhat better fits to individual lines can usually be achieved by varying slightly the assumed abundance table and $v \sin i$. However, even with the imposition of a single model, it is clear that there are no important errors in line shape. The standard line model reproduces these lines extremely well.

Note particularly that a non-zero microturbulent velocity is *not* actually detected in any of these three stars from the abundance analysis. Line profiles calculated assuming $\xi = 0$ are nearly identical to those shown in the figures.

We next consider whether it is possible to detect in the actual line profiles the presence of small microturbulent velocities through possible excess broadening or detailed study of line core shape. The main challenge is to distinguish microturbulent broadening from rotation. At such small values of $v \sin i$ the two effects produce very similar profiles. To try to detect directly the microturbulent component assumed in the model lines, the quality of fit of line profiles as a function of ξ (always using the best value of $v \sin i$ corresponding to each ξ) was studied for each of the stars studied.

For the two stars with relatively large $v \sin i$, 53 Tau and 21 Peg, the constraints on ξ that may be obtained directly from the line profiles (as opposed to deduction from abundance analysis) are not very useful. Line profiles with $v \sin i \approx 5$ and $\xi = 0$, and with $v \sin i = 0$ and $\xi = 3.5$ km s^{-1} both fit the individual profiles of 53 Tau equally well (although the profiles with large ξ require quite different assumed abundances for strong and weak lines), and from the profiles alone we derive only $\xi < 4$ km s^{-1}. Similarly, the strong line profiles of 21 Peg yield only an upper limit of $\xi < 3$ km s^{-1}. In both cases the upper limit on ξ derived directly from the profiles is considerably larger than the value obtained from abundance analysis.

However, for HD 193452, with its considerably narrower lines, the upper limit from the profile fits is more restrictive. For the strongest lines of Cr ($\lambda\lambda$ 4618 and 4634) even $\xi = 1$ km s^{-1} is slightly too large a value to obtain a good fit; the calculated profiles are a little too wide and shallow. Although even in this star I could not distinguish

Table 6. Spectral lines included in line synthesis (gf values adjusted astrophysically indicated by *)

ion	mult	λ(Å)	E_l(cm^{-1})	log gf
Cr I	21	4616.120	7927.47	-1.19
Cr II		4616.241	45730.578	-2.10*
Cr II	44	4616.629	32844.76	-1.36
Fe I	409	4618.757	23783.613	-2.95
Cr II	44	4618.803	32854.95	-0.84
Fe I	821	4619.286	29056.32	-1.12
Cr I	81	4619.530	24093.160	-0.59
Fe II		4619.628	62171.61	-1.89*
La II	76	4619.874	14146.	-0.14
Fe I	821	4619.286	29056.32	-1.12
Cr I	81	4619.530	24093.160	-0.59
Fe II		4619.628	62171.61	-1.89*
La II	76	4619.874	14146.	-0.14
Fe II	38	4620.521	22810.36	-3.23
Ce II	27	4624.892	8.	+0.00
Fe I	554	4625.044	26140.18	-1.34
Fe II	219	4625.481	63559.49	-1.87*
Fe II	186	4625.893	48039.09	-2.25*
Cr I	244	4625.918	31049.33	-0.49
Cr I	21	4626.174	7807.	-1.32
Ce II	1	4628.161	64.	+0.52
Fe II	219	4628.786	63272.98	-1.49*
Zr II	139	4629.07	20080.30	-0.51
Fe II	37	4629.339	22637.205	-2.33
Fe II	219	4631.873	63465.109	-1.65*
Cr II	44	4634.070	32844.76	-0.99
Fe II	186	4635.316	48039.090	-1.36
Fe I	554	4637.503	26479.377	-1.39
Fe I	822	4638.009	29056.320	-1.12
Fe II		4638.050	62171.613	-1.27*
Ni I		5168.656	29833.	-0.92
Fe I		5168.897	415.933	-3.97
Fe II		5169.033	23317.60	-1.04

between rotation and microturbulent velocities, the upper limit on ξ is small enough to fall well below the values of ξ of typically 2 km s^{-1} determined from abundance analyses of slightly cooler stars (e.g. Sirius and γ Gem in this study). The upper limit on ξ derived directly from the line profile shapes, about 1 km s^{-1}, is thus quite significant. It is very reassuring that it is consistent with the upper limit of about 0.7 km s^{-1} derived from the Blackwell diagram for Fe. In this star the two different methods agree very well on quite small upper limits for ξ.

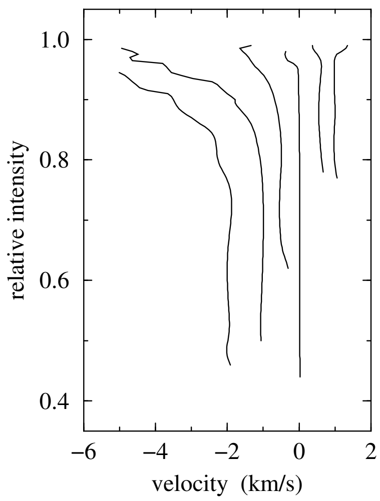

Fig. 5. Bisectors of the (typical) Cr II λ 4616 line, plotted on a velocity scale. The absolute horizontal position of each bisector has no significance; the bisectors have simply been separated for ease of plotting. From right to left, HD 27295 (53 Tau; T_e = 11800 K), HD 209459 (21 Peg; 10200 K), HD 193452 (10500 K), HD 72660 (9800 K), HD 108642 (8100 K), and HD 209625 (32 Aqr; 7900 K).

Another possible signature of a velocity field is the presence of line asymmetries, usually described in terms of the shape of the line bisector. The calculated bisectors for the (typical) Cr II λ 4616 line are shown for all the sharp-line stars in Figure 5. The bisectors of lines in these three stars are all essentially vertical; the lines are extremely symmetric, as may also be seen in Figures 2 – 4. The span (the real variation in velocity) of the bisectors is no more than about 0.2 km s^{-1}. The absence of any curvature of the bisectors is consistent with other evidence in pointing to velocity fields which have at most very small amplitude in the atmospheres of these stars.

5.3. The star HD 72660

Synthesis of HD 72660 has already been discussed briefly in section 4. This star is considered separately from the preceding three stars because, although its effective temperature is only a few hundred K below those stars, the abundance analysis unambiguously requires a non-zero microturbulent velocity of about 2.2 km s^{-1}. This is also true of Sirius, which has essentially the same T_e, and this change signals the abrupt onset on the main sequence of ξ values of well over 1 km s^{-1} at about 10000 K.

The Blackwell diagrams for Fe and Cr for this star (Fig. 1) define the value of $\xi = 2.2 \pm 0.1$ km s^{-1}. The values of $v \sin i$ deduced from the individual lines show systematic variations from a value below 5.2 km s^{-1} for the weakest lines up to 5.7 or 5.8 km s^{-1} for the strongest lines (Cr II $\lambda\lambda$ 4618 and 4634, and Fe II λ 4629). The fact that the mean value used for the final models, 5.6 km s^{-1}, is a little too large for the weaker lines is clearly visible in the figures. Nevertheless, the calculated profiles with a single model having the parameters given in Table 5 fit the observed profiles very well.

As was the case for 53 Tau and 21 Peg, the $v \sin i$ value of this star is sufficiently large that the profiles provide no strong constraint on the value of ξ. A value of 3 km s^{-1} fits the profiles almost exactly as well as a value of 0 km s^{-1}, except for the fact that the larger ξ value fits the outermost line wings a little better than the model with $\xi = 0$.

However, one further small but systematic discrepancy between the model lines and the observed lines occurs. The observed lines are noticeably asymmetric, with a long wavelength wing which is steeper than the short wavelength wing. This difference is greatest near the continuum, where blue wings of all the stronger lines show mild depression of the observed line profiles below the calculated profiles. This asymmetry is clearly visible in calculated line bisectors as well (the bisector plotted in Figure 5 is typical), which show a characteristic slant from longer wavelength at the line core to shorter wavelength near the continuum, with a span of about 1 km s^{-1}. It seems very likely that this asymmetry is related to the velocity field in the stellar atmosphere. *In HD 72660 we apparently directly detect evidence of a velocity field with characteristic velocity of the order of 1 km s^{-1}, corresponding to the deduced value of ξ of 2.2 km s^{-1}.*

I have also computed the bisectors for the broader-lined stars Sirius and γ Gem, which have effective temperatures and ξ values similar to those of HD 72660. For these stars the bisectors show no clear systematic trend or slope; apparently random variations of a few hundred m s^{-1}, which differ from one line to another, are superposed on generally vertical bisectors. Even the rather modest values of $v \sin i$ present in these stars seem to be enough to mask the behaviour of the line bisectors in spite of the high resolution and signal-to-noise ratio of the spectra.

5.4. The Am stars HD 108642 and 32 Aqr

Finally we consider the two metallic-line stars with effective temperatures close to 8000 K, HD 108642 and 32 Aqr (HD 209625). Visual inspection of the spectra of these two stars (see Figure 2, for example) immediately reveals a completely unexpected aspect of the line profiles, visible only because the projected rotation velocities are so low: the weaker lines are roughly Gaussian, while the strong lines have pronounced wings, deeper and more extended on the blue side than on the red side of the line. These characteristics suggest that the standard line profile model will not fit these stars very well.

When line profiles are fit to the individual lines, it is quickly found that most of the fits are quite poor for all reasonable choices of abundances, ξ and $v \sin i$, particularly for HD 108642. The calculated line profiles for all the stronger lines lack the extremely prominent broad wings of the observed lines. As a result, the selection of the best parameter values for each line by the synthesis programme on the basis of the smallest mean square difference between the observed and calculated lines depends somewhat on the width of the spectral window used for the comparison, and the meaning of the Blackwell diagram is not entirely clear. However, it is certain even with this ambiguity that very large differences in the abundances derived from weak and strong lines exist unless ξ is assumed to be of the order of 3.5 km s^{-1} or more. The Blackwell diagram for HD 108642, using a window for comparison of observed and calculated profiles that is 0.7 Å wide, is shown in Figure 1. Even at the value of ξ for which the derived abundances are most nearly concordant, the line to line differences appear somewhat larger than for the hotter stars.

The large differences in line widths and profiles between the weak and strong lines lead to considerable differences in best fit values of $v \sin i$ from one line to another. For 32 Aqr, the strong lines (Cr II $\lambda\lambda$ 4616, 4618, 4634 and Fe II $\lambda\lambda$ 4620 and 4629) are best fit by values of $v \sin i$ which lie between about 7.5 and 11.5 km s^{-1}, while the weakest lines (Fe II $\lambda\lambda$ 4625 and 4631) are best fit with $v \sin i$ which decrease from about 6 km s^{-1} down to about 1 km s^{-1} as ξ is increased from 0 to 5 km s^{-1}. At $\xi = 4$ km s^{-1}, the strongest lines are best fit with $v \sin i$ between 9 and 11.5 km s^{-1}, while the weakest lines require $v \sin i$ values between 1.5 and 3.5 km s^{-1}.

For HD 108642, the strongest lines (Cr II $\lambda\lambda$ 4618, 4634 and Fe II λ 4629) are best fit with $v \sin i$ in the range of 6.5 to 10.5 km s^{-1}, while the weakest lines are best fit with $v \sin i$ values that decrease from about 4.5 km s^{-1} down to 0.5 km s^{-1} or less as ξ is increased from 0 to 5 km s^{-1}. At a value of $\xi = 4$ km s^{-1}, the best fit $v \sin i$ values range from 9.7 (λ 4629) down to 0.2 km s^{-1} (λ 4631). It is clear that imposing a single value of $v \sin i$ and of ξ will lead to even worse fits to most of the lines than is the case when these are free parameters for each line.

The weak lines, which are narrow, provide valuable constraints on both $v \sin i$ and ξ for these stars. For HD 108642, the weak lines Fe II $\lambda\lambda$ 4625 and 4631 provide upper limits (at $\xi = 0$) of $v \sin i \leq 4.5$ km s^{-1}. Similarly, these lines provide upper limits (at $v \sin i = 0$) of $\xi \leq 3.5$ km s^{-1}. For 32 Aqr these two lines provide upper limits of $v \sin i \leq 6$ km s^{-1} at $\xi = 0$, and of $\xi \leq 4.5$ km s^{-1} at $v \sin i = 0$. Note that for 32 Aqr the upper limit on ξ derived directly from the weakest line profiles is only just consistent with the value inferred from the Blackwell diagrams, while for HD 108642 the upper limit on ξ is slightly *below* that derived from these diagrams.

The adopted model for 32 Aqr, shown in Figures 2 – 4, takes $\xi = 4.5$ km s^{-1} from the Blackwell diagrams and a value of $v \sin i \approx 1$ km s^{-1} determined from the weakest lines. Other parameters assumed in the model are shown in Table 5. While this method of parameter determination yields line profiles for the weakest lines that are not too far from the observed line profiles (except that the calculated profiles lack the strong wings observed in even the weakest lines), the strong lines are, as expected, very poorly fit. The model shown for HD 108642 in has been calculated using $\xi = 4$ km s^{-1}, even though this is not quite consistent with the weakest lines; from these lines a value of $v \sin i \approx 0$ is then derived. Again, this model fits the weak lines only moderately well, with discrepancies in the line wings, and fits the strongest lines extremely poorly.

It is clear that the standard model used to describe the spectral lines of these two stars, with its assumption of a height-independent microturbulent velocity field, is not a reasonable approximation for their atmospheres. It seems certain that the velocity field in these stars is detected, but that it differs very greatly from the one assumed in the model. Efforts are underway to find a description of the atmospheric velocity field that improves the agreement between observed and calculated lines, by incorporating variation of ξ with height, and large-scale flows (similar to radial-tangential macroturbulence), into the line profile computations. The results of these experiments will be reported in a future paper.

The bisectors of the strong spectral lines in these two stars vary somewhat from line to line, mainly because of blends, but all have essentially the same character, clearly visible in Figure 5: the bisector is nearly vertical in the line core, and then slants strongly towards the blue ("reversed C") in the upper part of the line. The overall span of the bisector is remarkably large, typically about 3 – 4 km s^{-1}. The largest values of bisector scan are found in the same stars for which the largest values of ξ, also around 4 km s^{-1}, are found.

The remarkable line shapes discovered in the spectra of these two very slowly rotating Am stars are not restricted to metallic line stars. Very similar spectral characteristics, namely strong lines that have strong bisector curvature and extended wings and that are significantly wider than the weaker lines, are found in the primary of the slowly rotating normal SB2 system HD 103578. This star is not discussed further in this paper because of the fact that it is an obvious SB2.

5.5. *Observations of the Fe II λ 5169 line*

In addition to the observations of the spectral region at 4630 Å, I observed several of the same stars in a spectral window at 5170 Å. The interest of this window is that it contains the Fe II line at 5169.033 Å, the strongest Fe II line in the visible spectrum. Because of the sensitivity of line cores of strong lines to the structure of velocity fields, it was hoped that observations of this line could provide further information about any velocity fields that might be present in the stars studied here.

The observations of this line (reported in Table 2) are all shown in Figure 6. As expected, the λ 5169 line is deeper and stronger than even the strongest lines in Figures 2 and 3. Damping wings are definitely present in the profiles of the two hottest stars observed, HD 193452 and 21 Peg.

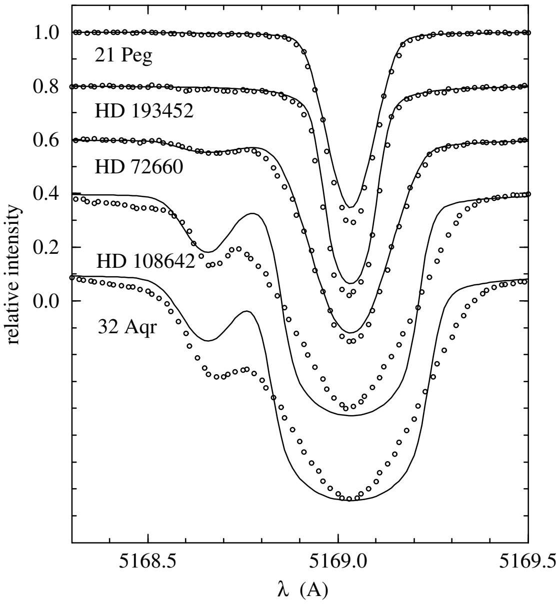

Fig. 6. Comparison of observed (dots) and calculated (solid lines) line profiles for the strong Fe II line λ 5169 Å. All observations have been shifted to the radial velocity frame of reference of the laboratory for ease of plotting. From top to bottom, the profiles are for HD 209459 (21 Peg), HD 193452, HD 72660, HD 108642, and HD 209625 (32 Aqr).

When the λ 5169 profiles of the three hottest stars observed (21 Peg, HD 193452, and HD 72660) are fit for a series of values of ξ, taking $v \sin i$ and $n(\mathrm{Fe})/n(\mathrm{H})$ as free parameters, we find in all three cases that the abundance inferred from this line at the value of ξ which best fits the remaining lines is 0.1 to 0.2 dex larger than the value required for the rest of the lines, even though (Table 4) the uncertainties in the gf values of the strong Fe II lines are small enough that it is doubtful that this difference is due to gf error. Thus, when the profile of this line is calculated using the parameters of Table 5 (abundance, $v \sin i$, and ξ) adopted for each star for other line profile calculations, the calculated profile of the λ 5169 line is always a little less deep than the observed line, and has wings which are slightly less deep than observed. This comparison is shown in Figure 6; the line profiles there have been computed with the same model used for all other lines. Better agreement in the far wings can be achieved by increasing all the damping constants from the values used (which were taken from Kurucz' GFIRON list) by about 0.1 dex, but this does not remove the systematic discrepancy between observed and calculated line cores. It may be that the core discrepancy is due to the gf value adopted for this line, but it is quite possible that this is an effect of departure from LTE high in the atmospheres of these stars.

Apart from the difference between calculated and observed core depths, the overall shapes of the λ 5169 line are very well fit for the two hot stars 21 Peg and HD 193452. The shapes of the calculated and observed line cores are very similar. No significant bisector curvature is observed in these lines. For HD 72660, the observed line core shape (but not the depth) is also well fit. However, the observed line profile has the same distortion relative to the calculated line that is observed in strong lines in the 4630 Å region: the observed long red line wing is slightly steeper than the calculated profile, while the observed blue line wing is slightly shallower than calculated, and the blue line wing near the continuum is significantly depressed compared to both the observed red wing and to the calculated line profile. This line has a bisector shape similar to those of the strong lines in the 4630 Å region, almost vertical deep in the line, then curving towards the blue near the continuum, with a span of approximately 1 km s^{-1}.

The behaviour of the Fe II 5169 Å line in the two Am stars HD 108642 and 32 Aqr parallels what we have already noted for the strong lines in the 4630 Å region. In the Blackwell diagram, this line indicates for the best-fitting value of ξ an abundance of Fe of 0.0 to 0.1 dex larger than that deduced from other lines. As expected, for values of ξ around the values selected in Table 5, the fit to the line profile is very poor. It is obvious from Fig. 6 that the theoretical profiles assuming a height-independent microturbulent velocity field do not represent the observed profiles adequately.

Because of the strong blending Ni I line in the blue wing of the Fe II λ 5169 line, it is not possible to compute bisectors for this line in the cool stars except in the line core, where the bisectors are similar to those found in the strong lines around 4630 Å.

6. Convection and the inferred velocity fields

We may summarize the main results of the preceding sections as follows. For stars with $T_e > 10000$ K, the observed line profiles are fit very well by the classical synthesis model. No significant velocity field is detected either directly from the profile shape or width, or indirectly from deduced microturbulence, with upper limits of order 1 km s^{-1}. For stars with 9000 K $< T_e <$ 10000 K, the classical synthesis model still fits the line profiles very well, but evidence for an atmospheric velocity field *is* directly detected both in the small distortion of the line profiles of HD 72660 and in the clearly non-zero microturbulent velocity parameter. The detected velocities are of the order of 1 – 2 km s^{-1}. Finally, for $T_e \approx 8000$ K, the standard line synthesis model is quite incapable of accounting for the observed profiles. These profiles appear to be greatly influenced by the atmospheric velocity fields, which are deduced from bisector span and the microturbulent parameter ξ to be of the order of 3 – 5 km s^{-1}.

We now examine the convection properties of the model atmospheres used to synthesize the observed spectral lines, in order to determine the extent to which the convection predicted by the usual mixing-length theory is consistent with the observed velocities. For this comparison, I calculated for each star the variation of both the actual temperature gradient $\nabla = (d \ln T / d \ln p)$ and of the adiabatic temperature gradient $\nabla_{ad} = (d \ln T / d \ln p)_{ad}$, with optical depth, to identify regions of convective instability. In these unstable regions, the typical velocity $\overline{v}$ of convective elements was then estimated following the treatment of Mihalas (1984, Sec. 7-3).

To obtain $\overline{v}$, it is necessary to calculate a number of thermodynamic functions in the model atmosphere, including the value of the specific heats per unit mass at constant volume $C_V = (\partial E / \partial T)_V$ and at constant pressure $C_p = (\partial H / \partial T)_p$ (here E is the internal energy and H is the enthalpy of the gas), the adiabatic gradient ∇_{ad}, the ratio of specific heats at constant volume and constant pressure $\gamma = C_p / C_V$, and the quantity $Q = -(\partial \ln \rho / \partial \ln T)_{P_g}$. These were computed using the method of Vardya (1965), but neglecting the (unimportant) contributions of metals and radiation energy density. At each unstable level in the atmosphere, the Rosseland optical depth of a characteristic convective element was estimated, and the temperature gradient ∇_E of the rising or falling element found from Eqn (7-76) of Mihalas. Finally, $\overline{v}$ was computed from Mihalas' Eqn (7-68).

The results of these computations are shown in Figure 7 for four typical stars, calculated for a ratio of mixing length ℓ to scale height H of 1.0. In each panel, I show the actual temperature gradient ∇ for the adopted model atmosphere compared to the adiabatic gradient ∇_{ad}, as a function of optical depth at 5000 Åτ_{5000}. Instability occurs where $\nabla > \nabla_{ad}$. In general, this condition is satisfied in regions of unusually high continuous opacity, which in the atmospheres in question occur where H or He is partly ionized, and the upper levels which contribute important bound-free continuous opacity are highly populated. To show this association, in each panel the (LTE) variation of the fraction of H which is ionized, $n_{H\,II}/n_H$ is shown. (A second region of weak instability, at somewhat higher value of optical depth than the region associated with partly ionized H, is due to the excitation of neutral He.)

For all the stars studied here, regions of instability are present near optical depth unity. However, the strength of the instability (measured by the difference $(\nabla - \nabla_{ad})$) rises rapidly with decreasing T_e from marginally unstable at $T_e = 11800$ K to *extremely* unstable at 8000 K.

The typical convective velocities depend not only on the value of $(\nabla - \nabla_{ad})$ but also on the Rosseland optical depth of a convective element (which controls how quickly it can exchange heat with its surroundings by radiation) and on the specific heat (which determines how much the temperature of the convective element changes for a given heat exchange). In the region just below the stellar at-

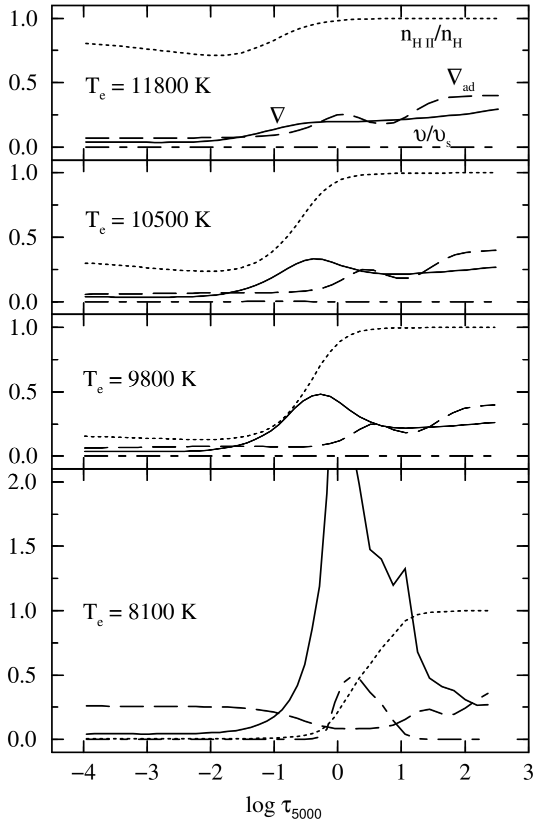

Fig. 7. Instability and convection in the atmosphere. Each panel shows for one star, as a function of optical depth, the fraction of H which is ionized (dotted), the actual temperature gradient $\nabla = (d \ln T/d \ln p)$ (solid) and the adiabatic temperature gradient $\nabla_{ad} = (d \ln T/d \ln p)_{ad}$ (dashed), and the mixing-length estimate of the velocity of convective elements relative to the local sound speed, $\overline{v}/v_s$ (dot-dashed). From top to bottom the panels show these quantities for 53 Tau, HD 193452, HD 72660, and HD 108642.

mosphere, both of these quantities increase rapidly with decreasing T_e. As a result, the typical convective velocities $\overline{v}$ predicted by the mixing length theory rise rapidly as T_e decreases. The computed velocities $\overline{v}/v_s$, relative to the sonic velocity v_s ($\approx$ 10 km s^{-1}), are shown in Fig 7. (All computations shown are for $\ell/H = 1.0$; the resulting convective velocity scales as $(\ell/H)^2$.) Only in HD 108642 and in 32 Aqr do the values of $\overline{v}$ rise to significant levels, up to about 5 km s^{-1}. In all the hotter stars, the computed value of $\overline{v}$ never exceeds $\sim 10^2$ m s^{-1}.

It thus seems that the simple mixing length model can account qualitatively for the presence of the large velocities observed in the coolest stars in the sample, and for the absence of detectable velocity fields for $T_e > 10000$ K, but does not predict the moderate velocities of order 2 km s^{-1} detected in stars in the temperature range 9000 K $< T_e <$ 10000 K. It is not clear physically why this intermediate temperature range should be described incorrectly by the mixing-length theory when its predictions are consistent with both adjacent regions.

7. Discussion

Finally, we look at the relationship between the results reported here and previous related studies. The only modern study of local line profiles in this spectral range is a study of Sirius by Dravins et al (1990) using spectra of similar resolution and but higher signal-to-noise ratio compared to my spectra of Sirius. The relatively large rotational broadening of the spectral lines of Sirius makes even the detection of the intrinsic line profile very difficult. However, from careful deconvolution, Dravins et al detect a Gaussian mean local profile with a full width at half maximum of about 8 km s^{-1}, comparable to the values reported in Table 1, which they cautiously interpret as reflecting the stellar velocity field. The weaker of the two lines studied seems fairly symmetric, but the stronger line appears to show a slightly depressed blue wing similar to what I observe in sharper-line stars. The observed profiles are compared to the calculations of Gigas (1989), but no other modeling is carried out.

Numerous other recent studies have, of course, modeled the observed line profiles of A and late B stars, but have generally *assumed* a form for the local line profile in order to extract other kinds of information from the observed profiles. This has been the case, for example, in efforts to model the magnetic geometry and abundance distributions of magnetic Ap stars (e.g. Landstreet 1988; Rice & Wehlau 1994; Wade et al 1996) and in the remarkable study by Gulliver et al (1994) revealing the rapid rotation of Vega via tiny distortions in line profiles.

Another kind of comparison of interest is with previous studies of spectral line bisectors. Bisector curvature among upper main-sequence stars has not been much studied. However, Gray & Nagel (1989) report a non-zero bisector slope in the Am (A8 V) star HD 3883. The sign of this slope is the same as that reported here for HD 72660, HD 108642 and 32 Aqr, but no amplitude is reported. Based on this star, and on observations of higher-luminosity stars, Gray & Nagel identify a "granulation boundary" in the H-R diagram, running from F0 on the main sequence to G1 for type Ib supergiants. On the hot side of this boundary they report that all stars appear to have line bisectors reversed with respect to the solar line bisector (which in Figure 5 would be almost vertical but with a small overall "C"-like curvature to the right). The present observations are consistent with the results of Gray & Nagel (see also Gray 1992), but extend the region of the main sequence for which data are available up to about B8. In the new data, we see that strong reversed bisector curvature is present in mid-A main sequence stars, diminishing to mild curvature (always with the same sign) at about A1 V, and vanishing completely at about A0 V. The present data thus extend the known size of the region of reversed line bisectors, and reveal at A0 the edge of another region in the H-R diagram apparently characterized by an absence of detectable velocity fields.

At still higher effective temperature, Smith & Karp (1978) have detected line asymmetries in τ Sco (spectral type B0 V, $T_e \approx 30000$ K) very similar to those seen here, with a depressed blue line wing and blue-curving bisectors having a span of order 1 km s^{-1}. They argue that this asymmetry is probably not due to a stellar wind, but to atmospheric motions driven by the He II ionization zone not far below the photosphere. They model their line profiles with a combination of rotation (5 km s^{-1}) and radial-tangential macroturbulence (6 km s^{-1}); a value of ξ of 3 km s^{-1} is deduced from a curve-of-growth analysis. This star appears to reveal yet another region on the main sequence where reversed bisectors appear again.

An outstanding feature of the bisectors found in the A stars is the large amplitude of velocity difference between line core and line wings (the velocity span). For stars later than about F5 V, the total variation of velocity of typical line bisectors is a few hundred m s^{-1} or less (Dravins 1987, Gray 1992). The bisector velocity excursions are larger in giants and especially supergiants, rising to about 2 km s^{-1}. Remarkably, the velocity span for the bisectors of the two mid-A main sequence stars studied here, which have a total span of 3 – 4 km s^{-1} (see Figure 5), are comparable to those the of super-giants.

It is probably not a coincidence that very large values of ξ and of bisector span appear as one descends the main sequence at essentially the same effective temperature, around 8000 K, where spectral evidence for the presence of chromospheres is first detectable in form of ultraviolet emission lines of ions (such as C II and III, Si III, N V, and O VI) which require relatively elevated temperatures for excitation (Walter et al 1995; Simon & Landsman 1997; Simon & Ayres 1998). These "transition region" lines are normally taken to be direct evidence for a chromosphere created by heating from the surficial convection zone for which I find strong evidence in the line profiles and ξ values; both effects are presumably produced by the strong buoyancy indicated by the stability diagram (Fig. 7) at this temperature.

The bisector curvature observed in stars is generally explained as being produced by the Doppler shifts and surface brightness variations of the rising and descending columns of gas in the stellar atmosphere. Empirical models of bisectors (parameterized models involving two to four gas streams moving with various velocities) have been developed, mostly for cooler stars, e.g. by Gray (1989) and Dravins (1990). It appears that the curvature of the solar bisectors reflects a surface convective structure characterized by relatively rapid and cool downflows covering a rather small fraction of the stellar surface (inter-granular lanes) and by larger areas of slower, warmer upflow (granules), perhaps together with horizontal flows and/or regions of little movement. This interpretation suggests that the reversed bisector curvature of A stars may be due to convective structure with relatively small areas of rapid upflow and larger areas of slow downflow, and in fact empirical models of Gray (1989) and of Dravins (1990) for stars with reversed bisectors have this character. This in turn suggests that the structure of convective movements in A star atmospheres is quite different from that in solar-type stars.

The convective structure of the atmospheres of A stars has not yet been extensively studied by hydrodynamic numerical simulation of the gas motions. However, two recent studies cast some light on such atmospheres. Gigas (1989) has studied the atmosphere of a star of $T_e = 9500$ K, $\log g = 3.90$ using a two-dimensional hydrodynamics code with cylindrical symmetry and grey radiative transfer. Unlike most numerical simulations of convective regions, which typically show evolving regions of concentrated downflows together with slower upflows, as well as large vortices, the simulations of Gigas yielded essentially vertical oscillatory motions. Because the character of the atmospheric motions is so different in these simulations from the results of other numerical models (perhaps because of the cylindrical symmetry assumed), it is not clear that this work has resulted in a realistic model of A-star convection. However, Gigas carried out line synthesis using his hydrodynamic models, and predicted that line profiles should show reversed bisector character comparable in amplitude and shape to the bisectors observed for HD72660. Unfortunately, he was not able to find in the numerical results a simple explanation of the predicted bisectors.

More recently, numerical models of A-star convection for $T_e = 8500$ K have been discussed by Freytag et al (1996). This work is based on a Cartesian two-dimensional hydrodynamics code with non-grey radiative transfer. The convection structures found with this code resemble much more closely than those of Gigas the kinds of convective motions found in other numerical simulations, giving one some confidence that the results may be usefully realistic. Unfortunately, no predicted line profiles are presented. However, the surface convection structure can be compared to that found for a solar atmosphere (an example is shown in the same paper). The convective structure appears very similar except for the fact that in the A-star convection carries almost none of the energy, and therefore has no effect on the isotherms. This result is somewhat puzzling, as it does not offer any obvious explanation as to why the bisectors of A-type stars should be reversed with respect to the solar bisector, since similar flow patterns (rapid downflow over small regions, slower upflow over larger regions) are found in both A-star and solar models. Nevertheless, the flow velocities found are similar in amplitude to those observed here.

It is clear that the direct detection of the signature of velocity fields in the spectral lines of A stars is indeed possible, and should be able to furnish significant constraints on models of atmospheric convection. Furthermore, significant tests of the local line profile calculated in spectrum synthesis are possible even in stars in which no velocity signature is detected. Both of these possibilities should facilitate improved understanding of the atmospheres of middle main sequence stars.

Acknowledgements. Much of the work of reducing the spectra was carried out by Stephen Arenburg, Peter Dimitroulos, and Nicole Harvie. Drs. G. Mathys and G. Wade obtained some of the spectra. Valuable comments on an earlier version of the manuscript were given by Drs. C. Catala, J.-F. Donati, T. Ryabchikova, and G. Wade, and the referee. The project has benefited from using the Linux operating system and its tools, IRAF, and the SIMBAD and VALD data bases. This work has been supported by the Natural Sciences and Engineering Research Council of Canada, and by the Centre National de la Recherche Scientifique of France.

References

Allen, C. W. 1973, Astrophysical Quantities, Athlone Press.
Babcock, H. W. 1958, ApJS 3, 141.
Baschek, B., Garz, T., Holweger, H., Richter, J. 1970, A&A 4, 229.
Boesgaard, A. M., Heacox, W. D., Wolff, S. C., Borsenberger, J., Praderie, F. 1982, ApJ 259, 723.
Bridges, J. M. 1973, in Stoll, I. (ed.) Proc. 11th Int. Conf. Phen. Ion. Gases. Czech. Acad. Sci. Inst. Phys., Prague, p. 418.
Dravins, D. 1987, A&A 172, 200.
Dravins, D. 1990, A&A 228, 218.
Dravins, D., Lindegren, L., Torkelsson, U. 1990, A&A 237, 137.
Freytag, B., Ludwig, H.-G., Steffen, M. 1996, A&A 313, 497.
Fuhr, J. R., Martin, G. A., Wiese, W. L. 1988, J. Phys. Chem. Ref. Data, 17, suppl. 4.
Gatewood, G., Gatewood, C. V. 1978, ApJ 225, 191.
Gigas, D. 1989, in Rutten, R. J., Severino, G. (eds.) Solar and stellar granulation, Kluwer Academic Publishers, p. 533.
Gillet, D. et al 1994, A&AS 108, 181.
Gray, D. F. 1989, PASP 101, 832.
Gray, D. F. 1992, The observation and analysis of stellar photospheres, 2nd edition, Cambridge University Press.
Gray, D. F., Nagel, T. 1989, ApJ 341, 421.
Guthrie, B. N. G. 1984, MNRAS 206, 85.
Gulliver, A. F., Hill, G., Adelman, S. J. 1994, ApJ 429, 81.
Heise, C., Kock, M. 1990, A&A 230, 244.
Hill, G. M., Landstreet, J. D. 1993, A&A 276, 142.
Kroll, S., Kock, M. 1987, A&AS 67, 225.
Kurucz R.L. 1993, Model atmosphere program ATLAS9 published on CD-ROM 13.
Landstreet, J. D. 1988, ApJ 326, 967.
Landstreet, J. D., Barker, P. K., Bohlender, D. A., Jewison, M. S. 1989, ApJ 344, 876.
Mihalas, D. 1984, Stellar atmospheres. W. H. Freeman & Co., San Francisco.
Moity, J. 1983, A&AS 52, 37.
Piskunov N. E., Kupka F., Ryabchikova T. A., Weiss W. W., Jeffrey C.S. 1995, A&AS 112, 525.
Rice, J. B., Wehlau, W. H. 1994, A&A 291, 825.
Roder, O. 1962, Zs. F. Ap., 55, 38.
Ryabchikova, T. A., Hill, G. M., Landstreet, J. D., Piskunov, N., Sigut, T. A. A. 1994, MNRAS 267, 697.
Sigut, T. A. A., Landstreet, J. D. 1990, MNRAS 247, 611.
Simon, T. Ayres, T. R. 1998, ApJ 500, L37.
Simon, T., Landsman, W. B. 1997, ApJ 483, 435.
Smalley, B., Dworetsky, M. M. 1994, poster paper presented at IAU General Assembly, the Hague, Holland.
Smalley, B., Dworetsky, M. M. 1995, A&A 293, 446.
Smith, M. 1971, A&A 11, 47.
Smith, M. A., Karp, A. H. 1978, ApJ 219, 522.
Vardya, M. S. 1965, MNRAS 129, 205.
Wade, G. A., Elkin, V. G., Landstreet, J. D., Leroy, J.-L., Mathys, G., Romanyuk, I. I. 1996, A&A 313, 209.
Wade, G. A., Donati, J.-F., Landstreet, J. D. 1998, in preparation.
Walter, F. M., Matthews, L. D., Linsky, J. L. 1995, ApJ 447, 353.
Wolff, S. C., Preston, G. W. 1978, ApJS 37, 371.
Wolnik, S. J., Berthel, R. O., Wares, G. W. 1971, ApJ 166, L31.